Failure mechanisms of corrugated sandwich panels under transverse three-point bending

Fukun Xia[a], P.J. Tan[b,*] and Dong Ruan[a,*]

[a] Department of Mechanical and Product Design Engineering, School of Engineering, Swinburne University of Technology, Hawthorn, VIC3122, Australia

[b] Department of Mechanical Engineering, University College London, Torrington Place, London WC1E 7JE, UK

*Corresponding authors. pj.tan@ucl.ac.uk and druan@swin.edu.au

ABSTRACT

The failure mechanism of corrugated sandwich panels under three-point bending is investigated experimentally and numerically using ABAQUS/Standard. Three dominant modes of failure, viz. face buckling, face yielding, and core buckling, previously reported by others, were also identified here and they were found to be affected by the face-sheet thickness, core height, and the corrugation angle of the panel. It will be shown that the deformation map, and regime boundaries, theoretically predicted previously by Valdevit et al. are valid only for restricted cases when the indenter and support pins are simultaneously located at a vertex; their prediction breaks down if this condition is not met and alternative failure maps will be developed here. The indenter nose shape (flat and cylindrical), size of the indenter and the location of indentation – these were not previously investigated by others - will be shown to play a significant role on the mode of failure that a panel subsequently develops.

Keywords: Corrugated sandwich panel; three-point bending; failure mechanism; parametric study; failure map.

1. INTRODUCTION

Sandwich panel, made of a low-density core and two thin skins, is widely employed in applications that require a combination of high structural rigidity and lightweight, such as in aerospace, watercraft, and rail [1–6]. Compared to its monolithic counterpart, a sandwich construction offers superior specific stiffness and strength to weight ratio. Corrugated sandwich panels, consisting of a triangular [7], trapezoidal [8], or curvilinear [9] core, are often preferred in many applications since they are straightforward to manufacture, typically through a welding route, and are particularly amenable to production scale-up [10]. They can also mitigate problems associated with humidity retention which is common in sandwich panels with a foam or honeycomb core and have important aerospace applications [11].

Understanding how corrugated sandwich panels deform, and fail, under three-point bending will lead to a better/efficient design that could resist higher transverse load and improved energy dissipation without increasing its weight. In practice, if a sandwich panel is manufactured by adhesively bonding two face-sheets to a core, the most common mode of failure is through interfacial debonding [12–14]. If, on the other hand, the bond is perfect so that debonding does not occur, then a panel will fail primarily through deformation of its face-sheets and/or the core material. In all metal sandwich panels, the face-sheets typically fail by yielding or local buckling (wrinkling) [15,16]. An additional mode of failure known as intra-cell dimpling can also develop – this occurs in regions of the face-sheet that are not bonded to the cell walls of the honeycomb core [17,18] – and is more common for large core cell size or very thin face-sheets. The mode of failure that develops in the sandwich core depends on the core architecture. A honeycomb core may fail in out-of-plane core shear, core indentation, and shear buckling [19]. For foam cores, the most common failure modes are core shear and core indentation [20–21]. By contrast, a corrugated core avoids out-of-plane core shear failure due

to its high shear strength; however, they can exhibit failure modes associated with buckling or yielding [22–24].

Lu et al. [25] reported four distinct modes of failure, viz. face yielding, face buckling, core yielding, and core buckling, for corrugated sandwich panel with one end fixed and the other loaded vertically, in a cantilever mode. Subsequently, Valdevit et al. [1] proposed the theoretical predictions of the failure mechanisms for the corrugated sandwich panel under both transverse and longitudinal bending. Under transverse loading, the analytical non-dimensional critical load corresponding to the different modes are as follows [1]:

$$\text{Face yielding: } \left(\frac{V^2}{EM}\right)_{FY} = \frac{\varepsilon_Y t_f}{l}\left(\frac{h_c}{l}+\frac{t_f}{l}\right) \tag{1}$$

$$\text{Core yielding: } \left(\frac{V^2}{EM}\right)_{CY} = \frac{\varepsilon_Y t_c \sin\theta}{l} \tag{2}$$

$$\text{Face buckling: } \left(\frac{V^2}{EM}\right)_{FB} = \frac{k_f \pi^2 \tan^2\theta}{48}\left(\frac{h_c}{l}+\frac{t_f}{l}\right)^{-1}\left(\frac{t_f}{l}\right)^3 \tag{3}$$

$$\text{Core buckling: } \left(\frac{V^2}{EM}\right)_{CB} = \frac{k_c \pi^2 \sin^3\theta}{12}\left(\frac{h_c}{l}+\frac{t_f}{l}\right)^{-2}\left(\frac{t_c}{l}\right)^3 \tag{4}$$

where V and M are the maximum shear force and bending moment of the panel, respectively; ε_Y and E are the yield strain and Young's modulus of the panel material, respectively; l is the half of the span; and, k_f and k_c are the buckling coefficients that depend on the rotational constraint offered by the adjoining members. Note that the failure mode of the panel is the mode that has the minimum non-dimensional critical loads. Valdevit et al. [1] provided conservative estimates of k_f and k_c, and made use of the aforementioned failure criteria to construct failure maps for corrugated sandwich panels under bending. Notwithstanding, the indenter nose shape, size, and location of indentation were not investigated in [1] even though they will be shown here to have a significant effect on the failure mode that develops. Under three-point bending, a sandwich panel typically undergoes both bending and local indentation.

The latter plays a significant role in the initiation of failure, but this was not previously considered in [1]. Here, in this paper, the effects of indenter nose shape, indenter size, and location of the indenter will be considered for corrugated sandwich panels subjected to three-point bending. The effects of panel geometry (size) and local indentation on the deformation mode that develops in corrugated sandwich panels are investigated using the finite element (FE) method. Experiments were conducted to validate the FE predictions and the validated FE models are used for parametric studies. Failure maps are constructed for various bending conditions (i.e., locations of indentation and indenter nose shapes).

2. EXPERIMENTS

2.1 Specimens

Corrugated sandwich panels were manufactured from solid block of aluminum alloy Al-5052 by wire cutting. The material properties of Al-5052 were obtained according to the ASTM standard E8/E8M-15a on a 50 kN MTS machine. The true stress-strain curves for four test coupons are shown in Figure 1. The average Young's modulus, yield strength, and hardening modulus are 75.4 GPa, 90.6 MPa, and 755.0 MPa, respectively.

Figure 2 shows the geometric configuration of the corrugated sandwich panel. The overall in-plane size of the panels is 250 × 60 mm^2. The face-sheet thickness (t_f), core web thickness (t_c), core height (h_c), and corrugation angle (θ) are 1.5 mm, 1.2 mm, 15.0 mm, and 45˚, respectively. Each panel has seven complete triangular unit cells for its core. Hereinafter, for convenience, we shall refer to each member as a strut, including the top/bottom face-sheets which can be considered to comprise of eight struts, joined together in a continuous manner by virtue of how they were manufactured.

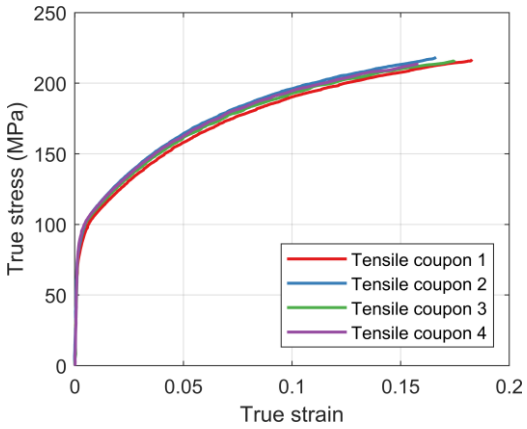

Figure 1. True tensile stress-strain curves of the aluminium alloy Al-5052.

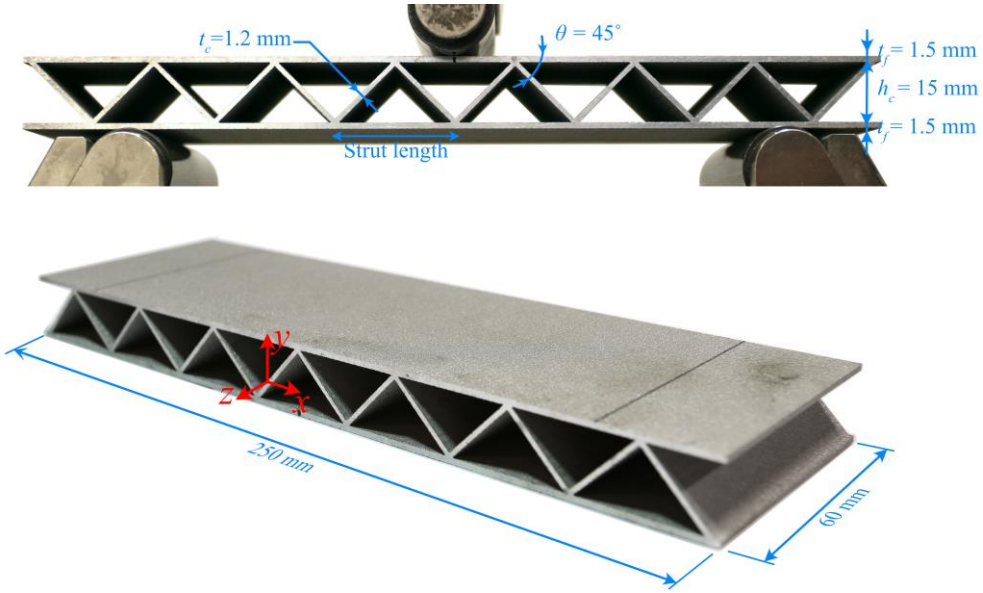

Figure 2. Photographs and dimensions of the corrugated sandwich panel.

2.2 Experiment set-up

Three-point bending tests were performed on a 50 kN MTS machine (model 43) using a bending fixture (model FWA105A). The diameter of the supports and indenter are 20 mm, and the span between the two supports was 150 mm. Tests were performed at a rate of 2 mm/min, and the applied load and indenter displacement were measured and recorded. The indenter was initially placed at the mid-point of the mid-strut (of the top face-sheet), as shown in the top image of Figure 2. Repeat tests were performed.

3. FINITE ELEMENT ANALYSIS (FEA)

3.1 FE models

Virtual simulations, identical to the experimental set-up, were performed using a finite element software (ABAQUS/Standard). Since the sandwich panel was cut from the same metallic block for the experiments, its 3D FE counterpart was also modelled by extruding a 2D sketch of both face-sheets and core. The material property used was provided in Figure 1. Both supports and the indenter were simulated as rigid bodies. Interactions between both the indenter/face-sheet and supports/face-sheet were simulated as surface-to-surface contact with a friction coefficient of 0.2. Since only small deformation was considered, the face-sheets do not come into contact the core during the simulations and, hence, no contact interactions were defined between the face-sheets and core to reduce computational cost. The two supports were fully fixed, and the indenter was constrained to move only along the out-of-plane direction (y-direction in Figure 2). Four-node shell elements (S4R), with five through-thickness integration points, were employed to mesh the panel. The supports and indenter were meshed by four-node rigid elements (R3D4). A mesh convergence study using mesh sizes of 3 mm, 2 mm, 1 mm, and 0.5 mm, was performed to determine the appropriate mesh size; a 1 mm mesh size was found to be a good compromise between computational cost and accuracy. In general, each member/strut was meshed with 20 S4R elements.

3.2 Failure criteria

The face-sheets and core may fail locally in various ways, viz. yielding, bending or buckling. Yielding – this can be caused by either axial stretch/compression or bending or their combination thereof – occurs when the local surface strain in any member exceeds the material's yield strain; the equivalent plastic strain (PEEQ) was used to determine the location at which material yielding first occurs. To capture buckling, the axial strain evolution on the

SPOS (surface positive) and SNEG of a member was employed (see schematic in Figure 3) to distinguish between bending and buckling deformation. The logarithmic strains (LE) of integration points 1 and 5 along the local *x* direction of an element (the default local *x* direction is the projection of the global *x* direction onto the surface [26]) are outputted as the strains on the SNEG and SPOS of the element at the centre of each strut (Figure 3). If a member deforms in bending, the axial strains on opposing surfaces (SPOS and SNEG) evolve to develop tensile and compressive strains simultaneously, in a manner shown schematically in Figure 3(a). By contrast, a buckling strut experiences the same initial compressive strain on both the SPOS and SNEG before bifurcating as shown in Figure 3(b).

By monitoring the axial strain evolution of all the struts in the FE model of the panel, it is possible to elucidate whether a panel fails initially by buckling or yielding – it is worth emphasizing that this can be caused by either stretch/compression or bending or their combination – in a strut. The mode of failure by the panel is categorized in accordance with the local failure first experienced by a strut in the core or the face-sheet, viz. face yielding, face buckling, core yielding, and core buckling.

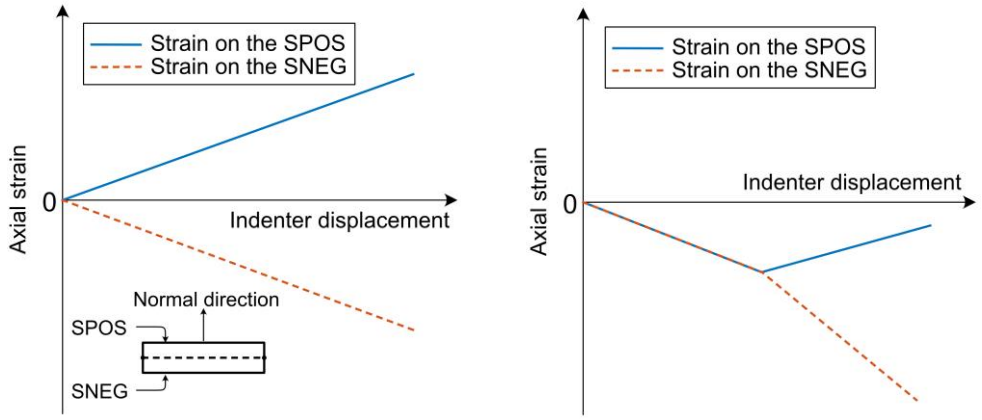

Figure 3. Schematic of the axial surface strain evolution on the SPOS (surface positive) and SNEG (surface negative) of a strut undergoing (a) bending versus (b) buckling.

4. RESULTS AND DISCUSSIONS

4.1 Experimental and FE results

In the experiments, the indenter is located slightly off the middle of the sandwich panel. This deviation in the experiments is approximately 1 mm for Sample 1 and 2 mm for Sample 2. Figure 4(a) shows a deformed corrugated sandwich panel under three-point bending when the indenter is 2 mm off the midpoint and the FE simulated deformation agrees well with that observed in the experiments. In general, the panel deformed globally under bending and experienced significant local indentation (beneath the indenter).

Figure 4(b) compares the load-displacement curves between experiments and those predicted by FE. Simulated results 1 and 2 are obtained from the FE models that the indenter is right on and 2 mm off the middle of the panel, respectively. In general, all four curves reach their peak loads at a displacement of approximately 1.2 mm. The two repeated experiments are largely in agreement with only small differences in their peak and plateau loads. Simulated result 2 agrees well with experimental result 2 because they have the same indenter location. Simulated result 1, of which the indenter is placed right in the middle of the panel, has the lowest load.

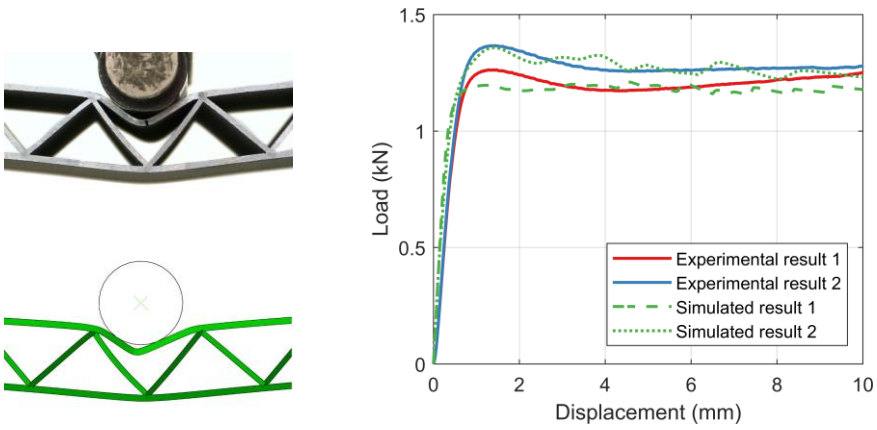

(a) (b)

Figure 4. (a) The comparison between the experiments and FE simulation: (a) deformation when the indenter displacement is 10 mm (top: experiment; bottom: simulation); (b) load-displacement curves.

4.2 Failure modes for cylindrical indenter

4.2.1 Indenter size

Additional simulations were also performed to establish how the indenter size affects the panel response – two additional indenter diameters of 10 mm and 30 mm were studied. The predicted load-displacement curves corresponding to three indenter diameters are plotted in Figure 5. At a small indenter displacement of, say, less than 1 mm, the three curves are almost identical, and the panel response is unaffected by indenter size. However, beyond 1.5 mm, significant differences are observed. Since the main purpose of this study is to characterize the deformation mode in the initial stage of deformation and indenter size has a negligible effect on the behavior of panels in this initial stage, a cylindrical indenter of 20 mm is employed in the discussion in this section (Section 4.2).

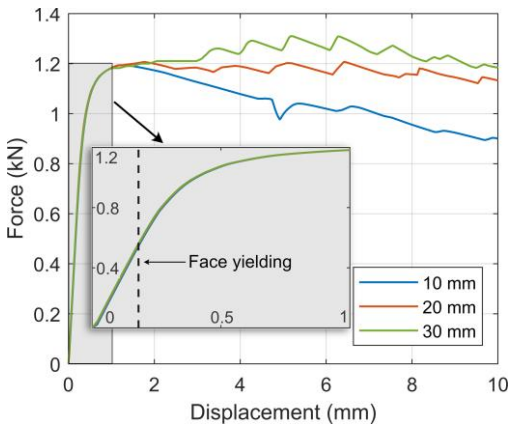

Figure 5. Predicted load-displacement curves for different indenter diameters.

4.2.2 Location of the indenter

Due to the discrete nature of the corrugated core, the location at which the indenter and supports contact the face-sheets will have a significant influence on the panel response and the mode of failure that it subsequently develops. In general, the load is higher if the indenter is located at the vertex, compared to when the indenter is located at any other location for a given indenter displacement [24]. Here, two loading scenarios based on the location of the indenter will be considered separately in the following sub-sections: node indentation (where the

indenter coincides with a vertex of a corrugation) and base indentation (the indenter is positioned anywhere else other than at a vertex).

4.2.2.1 Node indentation

Figure 6 shows the location of the indenter and supports. Here, both the indenter and the supports are located to coincide with a vertex of the corrugated core. For consistency with the work by Valdevit et al. in [2], we shall adopt their terminology and denote this loading configuration as node indentation Type NIA. Since the indenter and the supports are all located at the vertices, the strongest locations of a panel, local indentation is negligible in this indentation type. To achieve this loading configuration, the geometric parameters of the panel must satisfy the following relationship:

$$\frac{h_c}{\tan\theta}(2n+1) = l \quad (n = 1,2,3\cdots) \tag{5}$$

where n is a positive integer. A parametric study, using ABAQUS/Standard, was performed for this loading configuration. Four key parameters were considered: non-dimensional face-sheet thickness t_f/l non-dimensional core height h_c/l, corrugation angle θ, and non-dimensional mass m given by

$$m = \frac{2t_f}{l} + \frac{1}{\cos\theta}\frac{t_c}{l}. \tag{6}$$

Therefore, t_f/l should be between 0 and $m/2$.

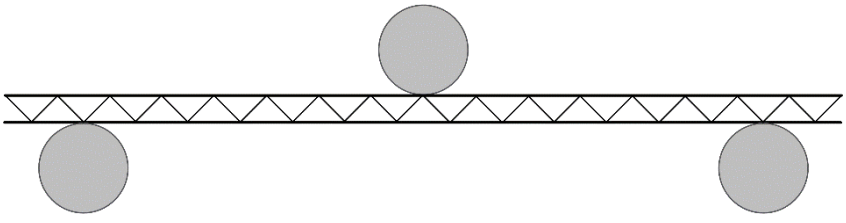

Figure 6. Schematic of node indentation Type NIA.

In the parametric study, θ, m, and l are kept constant, corresponding to 45°, 0.01, and 75 mm, respectively. A range of t_f/l (0.0005, 0.0015, 0.0025, 0.0035, and 0.0045) and h_c/l (1/23, 1/13, 1/9, 1/7, and 1/5) – this gives a total of 25 different combinations – were simulated. Three

failure modes, face buckling (Figure 7), face yielding (Figure 8), and core buckling (Figure 9), were predicted by the current FE simulations, and they are consistent with the theoretical predictions given in [2] as follows:

Face buckling: Figure 7(a) shows the equivalent plastic strain of a panel with $t_f/l = 0.015$ and $h_c/l = 1/7$ at an indenter displacement of 0.21 mm. Using the criterion described in Section 3.1, it is found that an element on the top face-sheet, indicated in red in Figure 7(a), has buckled at the indenter displacement of 0.036 mm (Figure 7b). The critical load corresponding to the onset of face buckling was found to be 12 N as shown in Figure 7 (c).

Face yielding: Figure 8(a) shows the simulated results for the panel with $t_f/l = 0.025$ and $h_c/l = 1/23$ at an indenter displacement of 1.18 mm. Yielding initiated in the top face-sheet under the indenter. The critical load of this panel was 80 N as shown in Figure 8(b).

Core buckling: Figure 9(a) shows the simulated results for the panel $t_f/l = 0.045$ and $h_c/l = 1/9$ when the indenter displacement is 0.16 mm. The core beneath the indenter buckled at the indenter displacement of 0.04 mm. The critical load was 21 N as shown in Figure 9(c).

It is worth highlighting that the critical load of all three panels are lower than their corresponding peak value in their respective load-displacement curve – the same is also reported by Valdevit et al. [2].

Results from the current FE simulations were combined with the analytical predictions of [1] into a deformation map as shown in Figure 10. The deformation map divides the two-dimensional (2D) geometric space into three regimes of deformation (face buckling, core buckling, and face yielding). The theoretical regime boundaries of [1] – correspond to equations. (1) to (4) in Section 1 – are shown as solid white lines. The color indicates the magnitude of the critical load corresponding to the first failure predicted by the current FE simulations. Yellow and blue colors represent the largest (187.7 N) and smallest (0.8 N) loads, respectively. In general, the mode of deformation predicted by Valdevit et al. [1] broadly agrees

with the present FE predictions. However, there are exceptions. The face yielding regime occupies a region greater than that predicted in [1]. It is also worth highlighting that the critical loads (predicted by FE and theory [1]) are the highest for combinations of geometric parameters in the vicinity where the three regime boundaries meet.

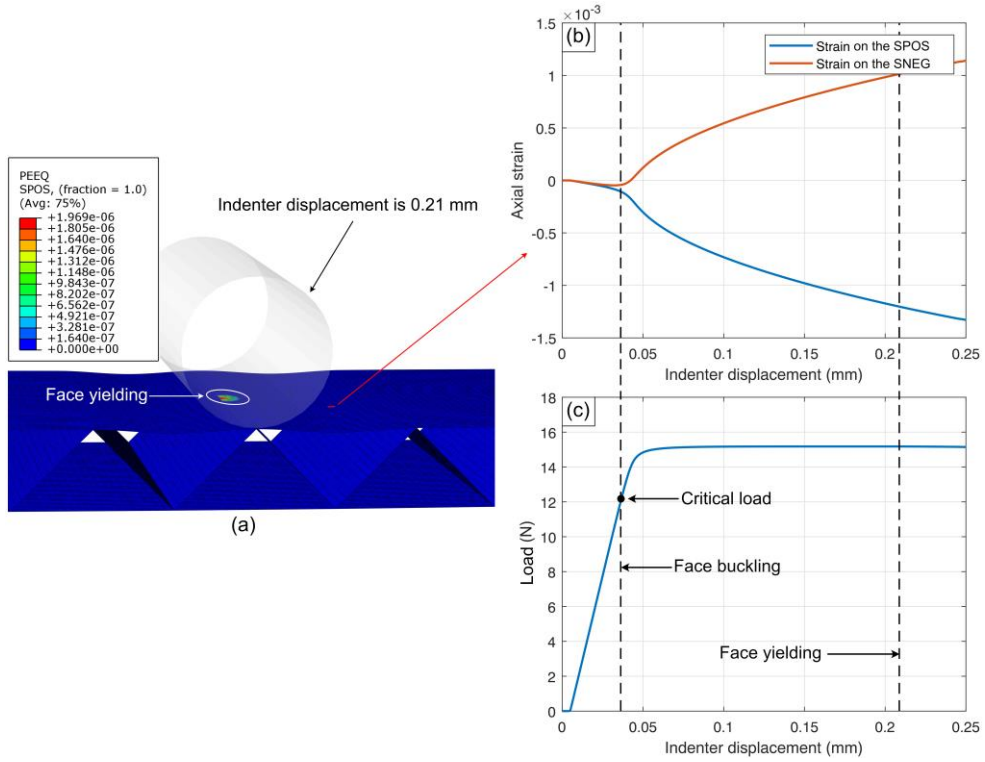

Figure 7. FE for a panel with t_f/l = 0.015 and h_c/l = 1/7: (a) equivalent plastic strain (PEEQ) at an indenter displacement of 0.21 mm; (b) axial surface strains on the SPOS and SNEG; and (b) load versus displacement curve.

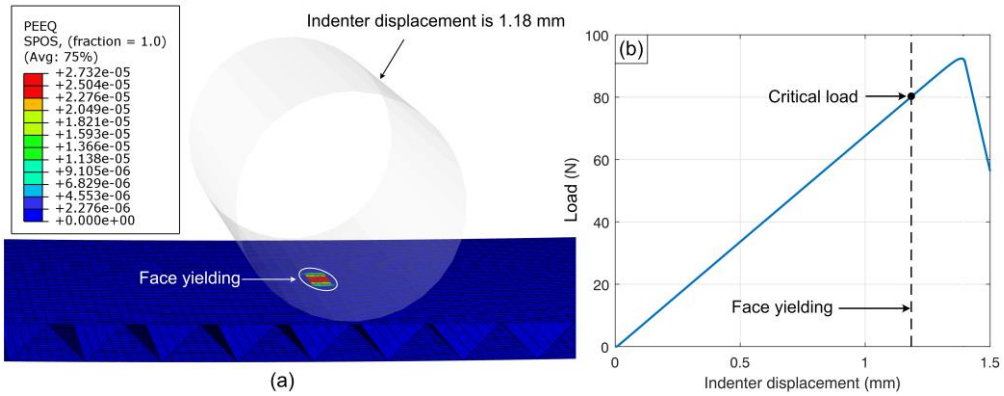

Figure 8. FE for a panel with t_f/l = 0.025 and h_c/l = 1/23: (a) equivalent plastic strain (PEEQ) at an indenter displacement of 1.18 mm and (b) load versus displacement curve.

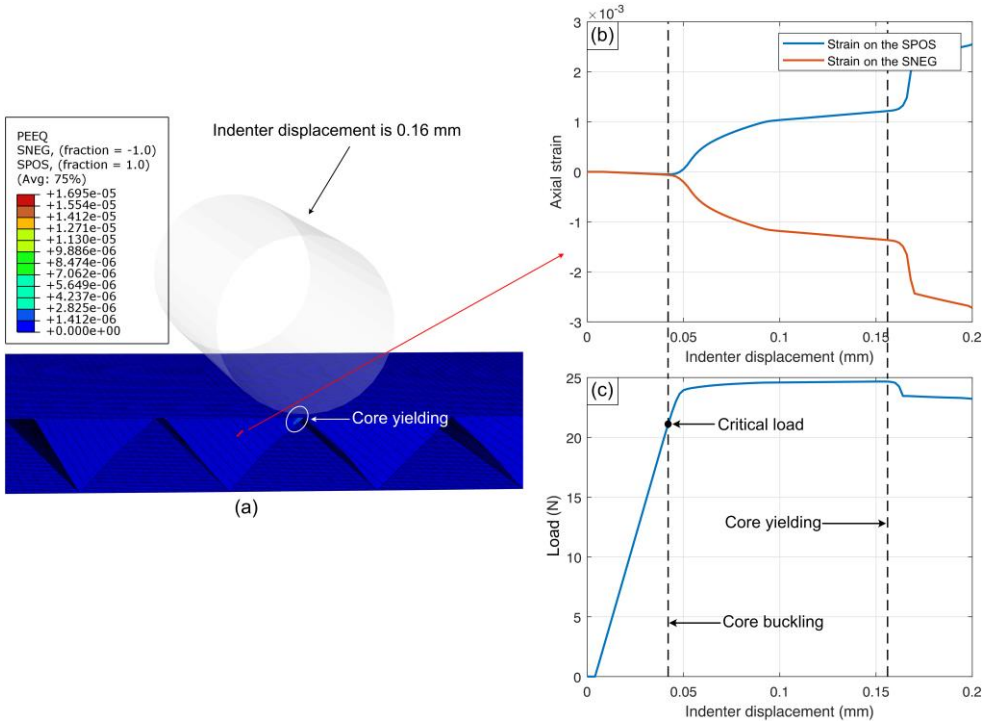

Figure 9. FE for a panel with t_f/l = 0.045 and h_c/l = 1/9: (a) equivalent plastic strain (PEEQ) at an indenter displacement of 0.16 mm; (b) axial surface strains on the SPOS and SNEG; and (c) load versus displacement curve.

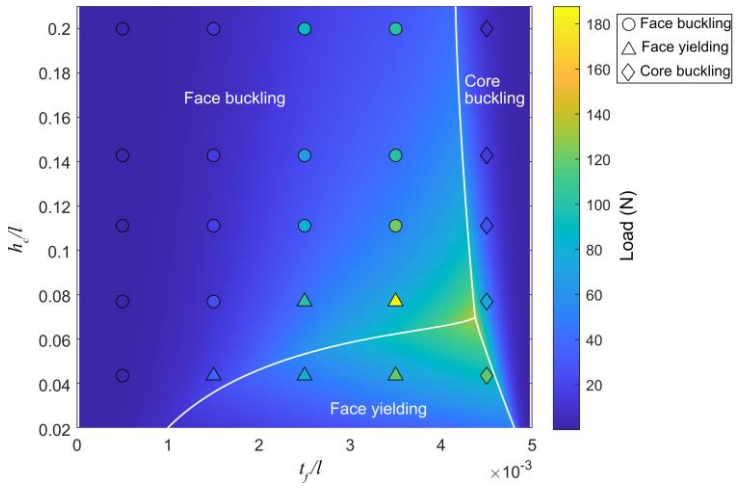

Figure 10. Deformation map for sandwich panels with θ = 45°, m = 0.01, and l = 75 mm. FE predictions are indicated by circle, triangle, and diamond symbols. Solid white lines are regime boundaries predicted in [2]. Color indicates the magnitude of the critical load.

The loading is classified as node indentation Type NIA only if the geometric parameters of a panel satisfy equation (5). In practice, however, this is unlikely to be the case and its consequence will be considered later. Therefore, there are certain regions in the deformation

map of Figure 10 that do not meet the criterion of Type NIA loading classification. Only selected geometric combinations of h_c/l and t_f/l – examples of these are highlighted as horizontal red dash lines in Figure 11(a), meet the geometric relation in equation (5). By contrast, the other h_c/l and t_f/l combinations correspond to a different loading classification to be introduced later. It must be emphasized that the red horizontal dash lines shown in Figure 11(a) are just a selection of the possible h_c/l and t_f/l combinations that satisfy equation (5) and there are more that were not shown.

More often than not, however, it is impossible to align the two supports with the vertices of the core, i.e. they are located anywhere between two adjacent vertices as shown in Figure 12. This loading configuration will be known here as node indentation Type NIB. Face yielding may occur either underneath the indenter or above the supports. Therefore, in addition to face yielding caused by global bending as described by equation (1), the local indentation above the supports must also be considered as follows. The face-sheet above a support can be regarded as a simply supported beam as shown in Figure 12. The maximum bending stress in the face-sheet between the two adjacent vertices *A* and *C* (shown in Figure 12) upon the support can be expressed as

$$\sigma_m = \frac{3F_B l_1(2h_c - l_1 \tan\theta)}{h_c t_f^2} \tag{7}$$

where

$$AB = l_1 = \left(l - \frac{h_c}{\tan\theta}\right) \bmod \left(\frac{2h_c}{\tan\theta}\right). \tag{8}$$

The non-dimensional critical load corresponding to face yielding for this loading scenario is the minimum stress caused by either global bending (equation 1 and the first term in the following equation) or local indentation (the second term in the following equation) given by

$$\left(\frac{V^2}{EM}\right)_{FY} = \min\left[\frac{\varepsilon_Y t_f}{l}\left(\frac{h_c}{l} + \frac{t_f}{l}\right), \frac{\varepsilon_Y h_c t_f^2}{3l_1 l(2h_c - l_1 \tan\theta)}\right]. \tag{9}$$

The non-dimensional critical load corresponding to the other three failure mechanisms (i.e., face buckling, core buckling, and core yielding) are only affected by global bending and, therefore, remains the same as given by equations (2), (3), and (4).

The theoretical failure map of the area corresponding to the regions between the two red dash lines h_c/l = 1/9 and 1/7 in Figure 11(a) is shown in Figure 11(b). Face yielding occupies the central region of the map, which is surrounded by the regimes of core buckling on the right and face buckling in the other area. The core buckling regime has shifted slightly compared to the map for node indentation NIA. However, a large region of the face buckling regime in Figure 11(a) is now replaced by face yielding caused by local indentation. Twenty five panels with a range of h_c/l (3/26, 3/25, 1/8, 3/23, and 3/22) and t_f/l (0.0005, 0.0015, 0.0025, 0.0035, and 0.0045) were simulated. The locations of the supports are at 1/6, 1/3, and 1/2 of a strut length from the nearest vertex as shown in Figure 13. The FE predictions are indicated by symbols (circle, triangle or diamond). Similar to the theoretical prediction, nine panels in the centre of the map fail via face yielding, and the greatest critical load is located near the intersection of the regime boundaries. However, the region corresponding to face buckling is larger than its theoretical counterpart – this is due to the simplified mechanical model of the face-sheet member in the derivation of equation (7).

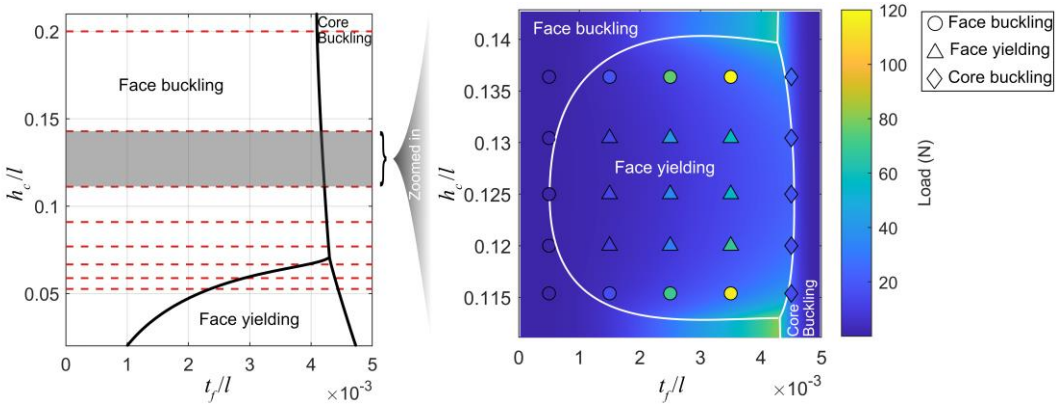

(a) (b)

Figure 11. Deformation map for θ = 45° and m = 0.01 corresponding to (a) node indentation NIA and (b) node indentation NIB. In (a), solid black lines are regime boundaries predicted in [1]. Solid red lines

represent combination of panel dimensions that satisfy equation (5). In (b), solid white lines are predictions by equation (2), (3), (4) and (9). FE predictions are indicated by symbols and color indicates the magnitude of the critical load.

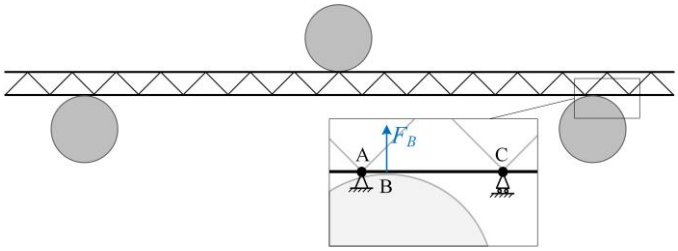

Figure 12. Schematic of the node indentation Type NIB.

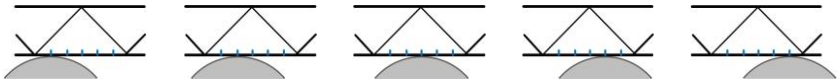

(a) (b) (c) (d) (e)

Figure 13. Locations of the right pin support when (a) h_c/l = 3/26, (b) h_c/l = 3/25, (c) h_c/l = 1/8, (d) h_c/l = 3/23, and (e) h_c/l = 3/22. The left and right pin supports are symmetric about the indenter.

4.2.2.2 Base indentation

There are only limited combinations of geometric parameters when both the indenter and supports are simultaneously located at the vertices. In practice, however, the indenter is likely to be located between two adjacent vertices as shown in Figure 14. This loading configuration is known as base indentation. Since the indenter and supports are not at the vertices and the load exerted by the indenter on the panel is always twice that of each support (to maintain static equilibrium), one can expect initial failure to occur in the vicinity of the indenter. Hence, the location of the supports, which can have a significant effect on the initial mode of failure, need not be considered for base indentation.

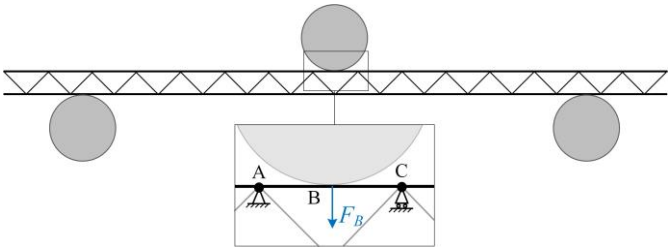

Figure 14. Schematic of base indentation.

Three different locations were investigated parametrically - at 1/6, 1/3 and 1/2 of a strut length between two adjacent vertices as shown in Figures 15(a), (b), and (c), respectively - to elucidate how the location of indentation affects the failure mode that develops. All the simulations were performed using panels with dimensions $m = 0.01$, $\theta = 45°$ and $l = 75$ mm. A range of non-dimensional face-sheet thicknesses (0.005, 0.015, 0.025, 0.035, and 0.045) and non-dimensional core heights (0.04, 0.08, 0.12, 0.16, and 0.20) were simulated. Unsurprisingly, they develop similar failure modes to those also observed in node indentation. Notice that the distribution of the failure modes within the 2D geometric space is identical for all three deformation maps and shown in Fig. 16. Unlike the case of node indentation Type NIA, face yielding is the more common deformation mode here. Since the results from the three indenter locations are largely similar, only the configuration shown in Figure 15(c) will be discussed in full and it may be representative of different indentation locations (within two adjacent vertices).

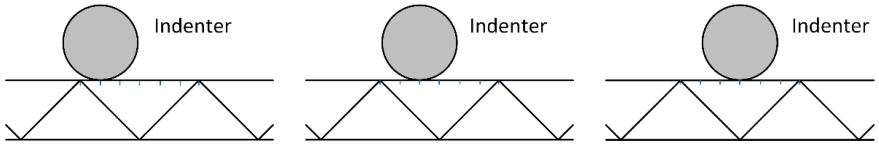

(a) (b) (c)

Figure 15. Location of the indenter at various distances from a vertex: (a) 1/6; (b) 1/3; and (c) 1/2 of a strut length.

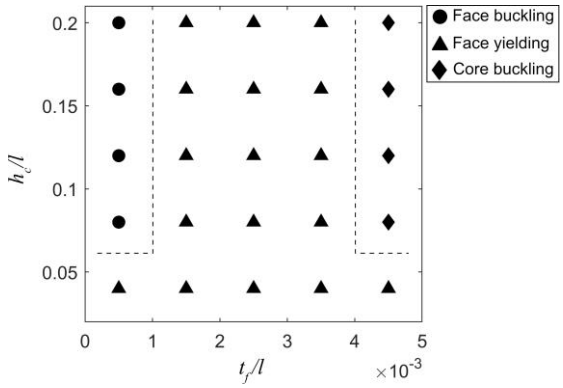

Figure 16. The failure map for different indenter locations shown in Figure 15.

The local indentation beneath the indenter can be simplified as shown in Figure 14. The maximum bending stress in the face-sheet between the two adjacent vertices *A* and *C* beneath the indenter and the modified non-dimensional critical force of face yielding can be expressed as follows:

$$\sigma_m = \frac{3F_B h_c}{t_f^2 \tan\theta} \tag{10}$$

and

$$\left(\frac{V^2}{EM}\right)_{FY} = \min\left[\frac{\varepsilon_Y t_f}{l}\left(\frac{h_c}{l}+\frac{t_f}{l}\right), \frac{\varepsilon_Y t_f^2 \tan\theta}{6h_c l}\right]. \tag{11}$$

The first term in equation (11) is the same as that in equation (1), arising from global bending, and the second term in equation (11) from local indentation.

Further simulations were performed to characterize how geometric parameters affect the failure mode and corresponding critical load for corrugated sandwich panels under base indentation. The parameters considered were m (0.01, 0.02, and 0.03), θ (30°, 45°, and 60°), t_f/l (m/20, 3m/20, m/4, 7m/20, and 9m/20), and h_c/l (0.04, 0.08, 0.12, 0.16, and 0.20). Note that l = 75 mm in all cases. A total of 225 different geometric combinations were simulated for the parametric study. The same three failure mechanisms were observed in all the cases. It is interesting to note that core yielding never occurred for any combination of parameters that were simulated. Figure 17 shows the FE predictions and the analytical regime boundaries as corrugation angle increases from 30° to 60°, and as the non-dimensional mass increases from 0.01 to 0.03. The maps obtained by simulations and analytical prediction are broadly in agreement with each other. In these maps, the majority panels fail by face yielding. Face buckling and core buckling occurs when the t_f/l is the minimum (m/20) and maximum (9m/20), respectively. Increasing either θ or m leads to a shift in the regime boundary so that those which previously failed by face buckling now do so by core yielding. However, the regime boundaries separating core yielding/core buckling and face buckling/core buckling are only marginally

affected by the corrugation angle and non-dimensional mass. Increasing θ leads to an increase in the corresponding critical load when m is fixed. In most of the maps, the highest critical load is found at the lower right corner of face yielding regime with one exception shown in Figure 17(d). Two different locations for face yielding were predicted as shown in Figure 18. Face yielding in Panel *M* occurred on the top face-sheet beneath the indenter and was caused by local indentation; by contrast, it occurred on the bottom face-sheet of Panel *N* as a result of global bending. Hence, the face yielding regime can be divided (analytically) into two subregimes as indicated by the dash line. The highest critical load can be found near the intersection of face yielding and core buckling regime boundaries.

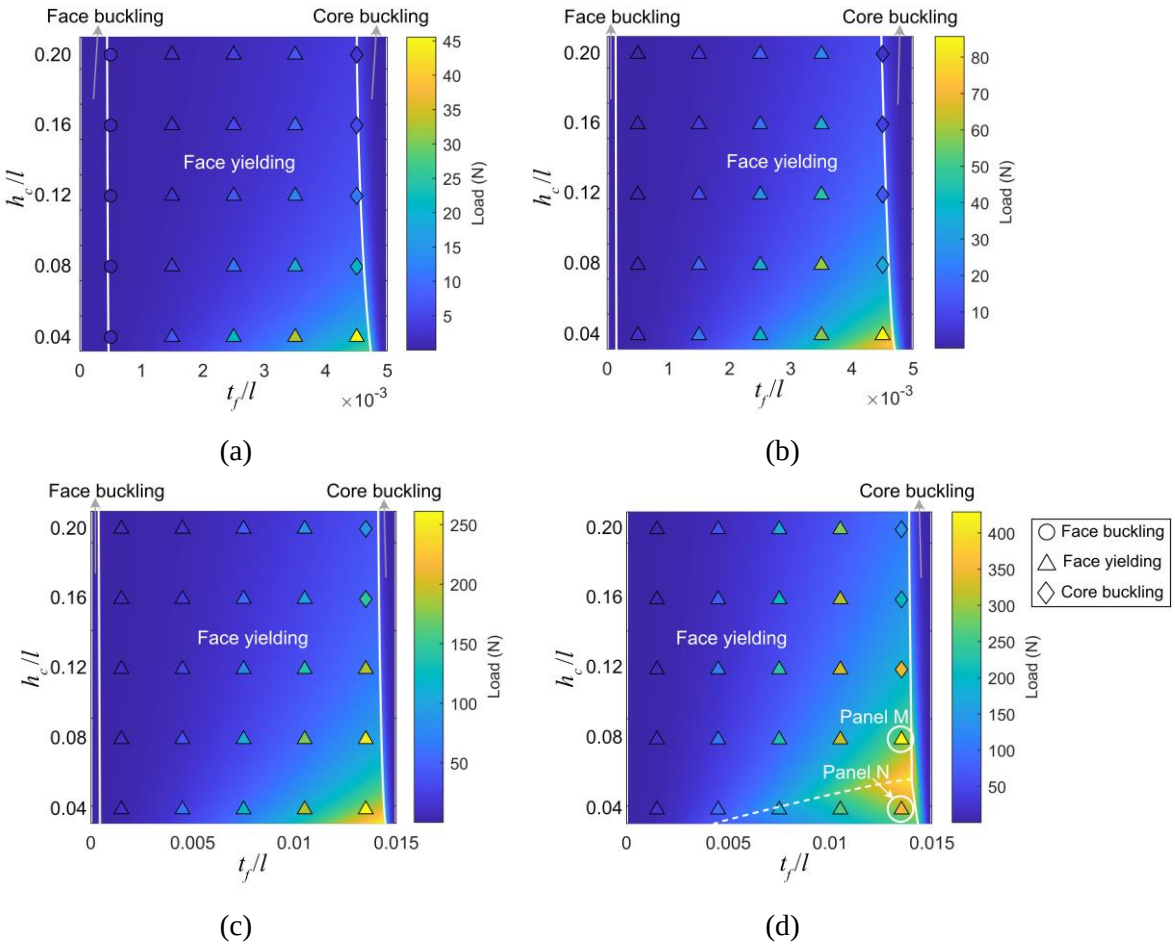

Figure 17. FE predictions and analytical regime boundaries for sandwich panels under base indentation: (a) m = 0.01, θ = 30°; (b) m = 0.01, θ = 60°; (c) m = 0.03, θ = 30°; and (d) m = 0.03, θ = 60°. Solid white lines are predictions by equations (2), (3), (4) and (11).

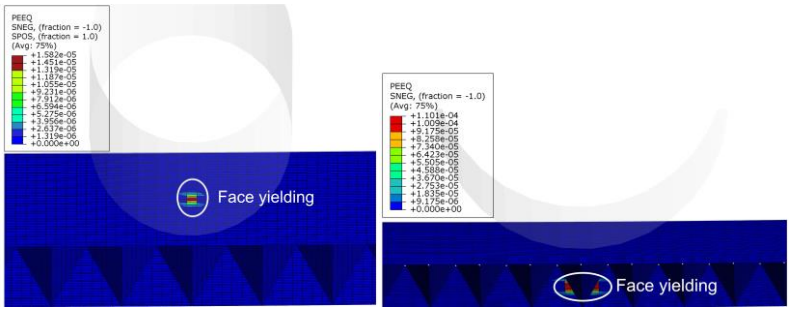

(a) (b)

Figure 18. Location of face yielding in (a) panel M and (b) panel N.

4.3 Failure modes for flat-ended indenter

If a flat-ended indenter is used in place of the cylindrical one, the contact area between the indenter and panel remains nominally the same with indenter displacement. It is of interests to understand how this affects the failure mode(s) compared to its cylindrical counterpart. Here, three flat-ended indenters, with widths at 0.5, 1, and 1.5 times of a typical struct length, were simulated investigated, see Figure 19. To ensure that deformation initiates near the indenter rather than at supports, the supports were placed at the vertices of the panel. Therefore, the geometric parameters of the panel must satisfy the following equation:

$$\frac{2nh_c}{\tan\theta} = l \quad (n = 1,2,3\cdots) \tag{12}$$

where *n* is a positive integer.

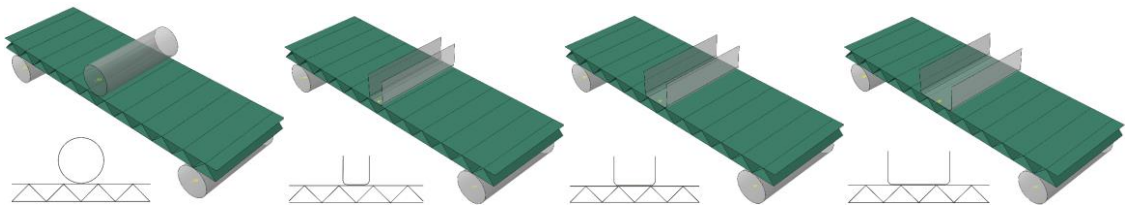

(a) (b) (c) (d)

Figure 19. Schematic of the corrugated sandwich panels under three-point bending with: (a) cylindrical indenter (diameter=20 mm); (b) flat-ended indenter whose width is half the strut length; (c) flat-ended indenter whose width is equal to a strut length; (d) flat-ended indenter whose width is 1.5 times the strut length.

To investigate the effects of indenter nose shape and size, three panels whose geometric parameters satisfy equation (12) were selected – this indicates that the supports are placed at

the vertices. These three panels failed by face buckling (m = 0.01, θ = 45°, t_f/l = 0.0005, and h_c/l = 0.1), core buckling (m = 0.01, θ = 45°, t_f/l = 0.0025, and h_c/l = 0.1), and face yielding (m = 0.01, θ = 45°, t_f/l = 0.0045, and h_c/l = 0.1) when a cylindrical indenter was used in Section 4.2.2.2. Figure 20 shows the load-displacement curves of the aforesaid subjected to three-point bending using different indenters. The vertical dashed lines indicate the displacement corresponding to failure for each case. Figure 20 (a) shows that face buckling occurs at 0.50 mm, 0.03 mm, and 0.03 mm for a flat-ended indenter whose width is 0.5, 1.0, and 1.5 times of strut length, respectively; by contrast, this occurs much earlier at 0.84 mm for a cylindrical indenter. In Figures 20 (a) and (b), the mode of failure that developed is identical for both the cylindrical and flat-ended indenters; in general, failure occurs at a lower indenter displacement (i.e., earlier in the indentation process) with increasing width of the flat-ended indenter. Interestingly, see Figure 20(c), if the indenter is cylindrical or flat-ended with a width one-half of the core length, then it fails by face yielding; if, on the other hand, the flat indenter's width is 1.0 or 1.5 times of the strut length, it fails by face buckling. When the indenter width is greater than or equal to the strut length, the indenter comes into contact with one or more vertices which retards the local indentation that would otherwise develop.

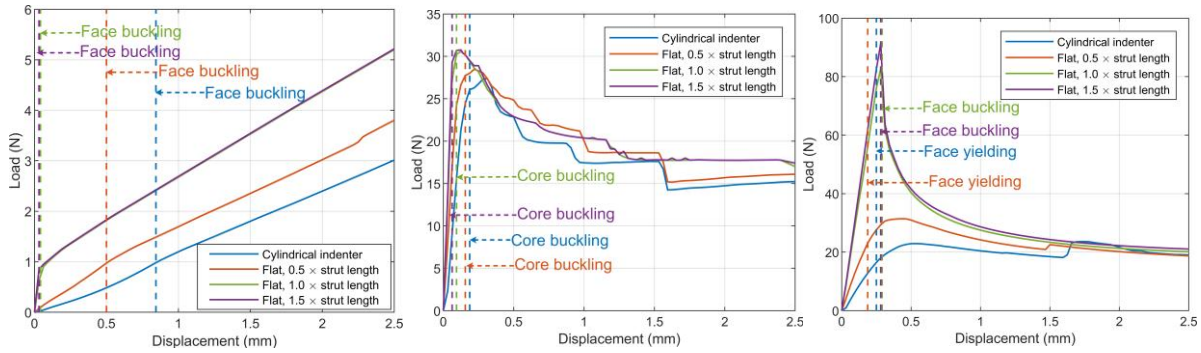

(a) (b) (c)

Figure 20. Load-displacement curves by different indenter nose shape for panel geometries: (a) m = 0.01, θ = 45°, t_f/l = 0.0005, and h_c/l = 0.1; (b) m = 0.01, θ = 45°, t_f/l = 0.0025 and h_c/l = 0.1; (c) m = 0.01, θ = 45°, t_f/l = 0.0045, and h_c/l = 0.1.

Figure 21 shows that the failure mode of the panel is the same when the indenter width is equal to or 1.5 times of the strut length. Therefore, parametric studies were only performed for

two cases, i.e. when the indenter width is either half or 1.5 times of the cell length. The parameters m, θ, and l are 0.01, 45°, and 75 mm. Notice that the failure maps for the cylindrical indenter and flat-ended indenter with a width of one-half the cell length are identical to the map shown in Figure 16 where face yielding is the dominating mechanism. Face buckling and core buckling occur only when the face-sheet thickness is at its minimum and maximum, respectively. By contrast, in Figure 21, face buckling is the dominant mode of failure for the majority of panels simulated. The failure map of the three-point bending using a flat indenter with a width of 1.5 times the strut length is identical to that for node indentation Type NIA shown in Figure 10.

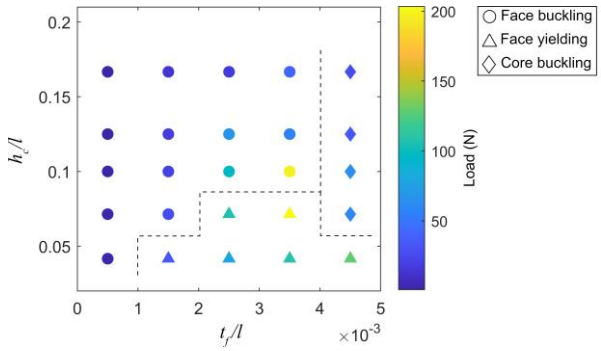

Figure 21. Deformation maps for a flat-ended indenter whose width is 1.5 times the strut length. Parameters m and θ of the panels are 0.01 and 45°, respectively.

5. CONCLUSIONS

Three-point bending experiments were performed for corrugated sandwich panels with selected geometries, and a detailed parametric investigation was performed to elucidate the influence of indenter nose-shape, locations of the indenter/supports, and geometric parameters on the mode of failure that develops. Similar failure modes (face buckling, face yielding, and core buckling) to that reported in [1] were also observed here. The failure mode induced by a cylindrical indenter is highly sensitive to the location of indentation and the support pins (whether they coincide with a vertex or not). Only when the indenter and support pins were simultaneously located at a vertex does the failure mode match that predicted by Valdevit et al. [1]. Alternative failure maps were developed for cases when the aforementioned condition is

not met. The indenter location was found not to have a significant effect on the regime boundaries of the new failure maps, where the dominant failure mode remains face yielding. Panels with thicker face-sheets tend to fail by core buckling. Increasing corrugation angle and non-dimensional mass leads to a switch from face buckling to face yielding, but both have a negligible effect on core buckling. If the width of a flat-ended indenter is one-half of a strut length, the failure map is similar to that for a cylindrical indenter which is non-coincident with a vertex. If the indenter width is either 1.0 or 1.5 times of a strut length, then failure map is similar to that for cylindrical indenter where the indenter and support pins were simultaneously located at a vertex.

ACKNOWLEDGEMENTS

The first author gratefully acknowledges the support from the Rail Manufacturing Cooperative Research Centre (funded jointly by participating rail organizations and the Australian Federal Government's Business Cooperative Research Centres Program) through a postgraduate scholarship.

REFERENCES

[1] L. Valdevit, J.W. Hutchinson and A.G. Evans. Structurally optimized sandwich panels with prismatic cores. *Int J Solids Struct* 2004; 41: 5105–5124.

[2] L. Valdevit, Z. Wei, C. Mercer, et al. Structural performance of near-optimal sandwich panels with corrugated cores. *Int J Solids Struct* 2006; 43: 4888–4905.

[3] C.E. Harris, J.H. Starnes and M.J. Shuart. An assessment of the state-of-the-art in the design and manufacturing of large composite structures for aerospace vehicles. *NASA Tech Memo* 2001; 39: 1–24.

[4] B. Metschkow. Sandwich panels in shipbuilding. Polish Marit Res 2006: 5–8.

[5] A. Wahrhaftig, H. Ribeiro, A. Nascimento, et al. Analysis of a new composite material

for watercraft manufacturing. J Mar Sci Appl 2016; 15: 336–342.

[6] J.S. Kim, S.J. Lee and K.B. Shin. Manufacturing and structural safety evaluation of a composite train carbody. *Compos Struct* 2007; 78: 468–476.

[7] N. Dahiwale, S. Panigrahi and K. Akella. Numerical analyses of sandwich panels with triangular core subjected to impact loading. *J Sandw Struct Mater* 2015; 17: 238–257.

[8] P. Zhang, J. Liu, Y. Cheng, et al. Dynamic response of metallic trapezoidal corrugated-core sandwich panels subjected to air blast loading - An experimental study. *Mater Des* 2015; 65: 221–230.

[9] T. Boonkong, Y.O. Shen, Z.W. Guan, et al. The low velocity impact response of curvilinear-core sandwich structures. *Int J Impact Eng* 2016; 93: 28–38.

[10] F. Côté, V.S. Deshpande, N.A. Fleck, et al. The compressive and shear responses of corrugated and diamond lattice materials. *Int J Solids Struct* 2006; 43: 6220–6242.

[11] M.R.M. Rejab and W.J. Cantwell. The mechanical behaviour of corrugated-core sandwich panels. *Compos Part B Eng* 201; 47: 267–277.

[12] Y. Yu, L. Ying, W. bin Hou, et al. Failure analysis of adhesively bonded steel corrugated sandwich structures under three-point bending. *Compos Struct* 2018; 184: 256–268.

[13] B. Du, L. Chen, J. Tan, et al. Fabrication and bending behavior of thermoplastic composite curved corrugated sandwich beam with interface enhancement. *Int J Mech Sci* 2018;149: 101–111.

[14] Y. Hu, W. Li, X. An, et al. Fabrication and mechanical behaviors of corrugated lattice truss composite sandwich panels, *Compos Sci Technol* 2016; 125: 114–122.

[15] T.C. Triantafillou and L.J. Gibson. Failure mode maps for foam core sandwich beams. *Mater Sci Eng* 1987; 95: 37–53.

[16] G. Li, Y. Fang, P. Hao, et al. Three-point bending deflection and failure mechanism map of sandwich beams with second-order hierarchical corrugated truss core. *J Sandw Struct*

Mater 2017; 19: 83–107.

[17] A.Petras and M.P.F. Sutcliffe. Failure mode maps for honeycomb sandwich panels. *Compos Struct* 1999; 44: 237–252.

[18] J.P. Vitale, G. Francucci, J. Xiong, et al. Failure mode maps of natural and synthetic fiber reinforced composite sandwich panels. *Compos Part A Appl Sci Manuf* 2017; 94: 217–225.

[19] X. Wei, Q. Wu, Y. Gao, et al. Bending characteristics of all-composite hexagon honeycomb sandwich beams: experimental tests and a three-dimensional failure mechanism map. *Mech Mater* 2020; 148: 103401.

[20] T.M. McCormack, R. Miller, O. Kesler, et al. Failure of sandwich beams with metallic foam cores. *Int J Solids Struct* 2001; 38: 4901–4920.

[21] H. Bart-Smith, J.W. Hutchinson and A.G. Evans. Measurement and analysis of the structural performance of cellular metal sandwich construction. Int J Mech Sci 2001; 43: 1945–1963.

[22] J.L. Yu, E. Wang, J. Li, et al. Static and low-velocity impact behavior of sandwich beams with closed-cell aluminum-foam core in three-point bending. *Int J Impact Eng* 2008; 35: 885–894.

[23] K. Mohan, Y. Tick Hon, S. Idapalapati, et al. Failure of sandwich beams consisting of alumina face sheet and aluminum foam core in bending. *Mater Sci Eng A* 2005; 409: 292–301.

[24] F. Xia, Y. Durandet, T.X. Yu, et al. Large deformation of corrugated sandwich panels under three-point bending. *J Sandw Struct Mater* 2021; 23: 3336–3367.

[25] T.J. Lu, J.W. Hutchinson and A.G. Evans. Optimal design of a flexural actuator. *J Mech Phys Solids* 2001; 49: 2071–2093.

[26] Manual, A.U. *Abaqus User Manual*; Abacus: Waltham, MA, USA, 2020.